processes

Article

Study on Dust Suppression of Air Curtain Soft-Sealing System of Grab Ship Unloader

Hanzhong Zhang [1,2,*] and Wenjun Meng [1,2,3,*]

1 School of Mechanical Engineering, Taiyuan University of Science and Technology, Taiyuan 030024, China
2 Shanxi Key Laboratory of Intelligent Logistics Equipments, Taiyuan 030024, China
3 Shanxi Institute of Energy, Jinzhong 030600, China
* Correspondence: tyustzhz@163.com (H.Z.); tyustmwj2022@163.com (W.M.); Tel.: +86-182-3403-3149 (H.Z.)

Abstract: In order to suppress the irregular diffusion of dust in the unloading process of grab ship unloaders, an air curtain soft-sealing system was designed that can effectively block the air flow and restrict the diffusion of pollutants and reduce the average mass fraction of pollutants outside the air curtain plane by 70.02%. The grab unloading model was constructed using the Computational Fluid Dynamics–Discrete Element Method (CFD-DEM) coupling method, and the diffusion law of the gas–solid two-phase flow field of the falling bulk material was studied. Moreover, the motion trajectory and velocity distribution of the particle flow field and air flow field were obtained, as well as the maximum air flow field velocity of five planes above the hopper. The three-dimensional model of the air curtain jet was used and simplified, and the air curtain parameters were set based on the maximum air flow field velocity. The barrier performance of the air curtain under different air curtain jet modes, jet widths, jet velocities and induced wind velocities was simulated by the control variable method. The results show that selecting the appropriate jet widths and jet velocities can significantly reduce dust diffusion; under different jet modes, the order of influence was blow and suction, unilateral blowing and bilateral blowing; under a certain range of induced wind velocities, the air curtain had an obvious blocking effect. These results can provide a reference for the design and improvement of dust suppression of the air curtain soft-sealing system.

Keywords: air curtain; grab ship unloader; dust; gas–solid two-phase flow; CFD-DEM coupling; CFD; barrier performance

check for updates

Citation: Zhang, H.; Meng, W. Study on Dust Suppression of Air Curtain Soft-Sealing System of Grab Ship Unloader. *Processes* **2022**, *10*, 1505. https://doi.org/10.3390/pr10081505

Academic Editor: Blaž Likozar

Received: 8 July 2022
Accepted: 27 July 2022
Published: 29 July 2022

1. Introduction

Grab ship unloaders are the leading mechanical equipment for bulk barges and seagoing ships. The overall structure, which consists of trusses, grabs, hoppers, trolleys and other components, is shown in Figure 1. The operation process is as follows: the grab grabs the materials from the cabin, runs to the top of the hopper through the trolley, then opens the grab to unload, and the materials are sent to the dock belt conveyor through the hopper, feeding device and material transfer device. During the unloading operation of grab, fine particles are entrained in bulk materials, which easily diffuse into the air and form dust. Moreover, the intermittent loading and unloading mode of grab makes it impossible to adopt fixed sealing. Therefore, it is necessary to take targeted measures to suppress dust diffusion.

The typical dust control methods in the material transfer process are used for water, water spray and ventilation dust removal. Different dust control methods have their own characteristics. Water has the advantages of simple and effective dust suppression and a low cost, but this leads to significant water consumption, which often causes runoff sewage and material caking in a low-temperature environment, and is not suitable for cement, grain or other dry materials. The water spray dust suppression effect is good, but the cost is high, the nozzle is prone to blockage and corrosion deformation, and it often makes the material damp. Ventilation dust suppression has broad applicability for materials and strong control over dust, but it requires high airtightness and energy consumption for the dust removal space, and the dust removal efficiency is low in an open environment. Considering the limitations of the above dust control methods, air curtain technology is innovatively adopted to form a soft-sealing barrier between the dust area and the clean area to inhibit dust diffusion.

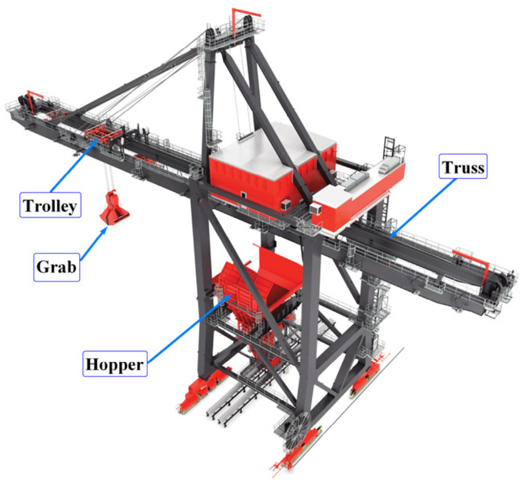

Figure 1. Three-dimensional model of grab ship unloader.

The air curtain was pioneered by Tephilus van kemmel to block heat exchange. In recent years, air curtain partition technology has been widely used in the fields of air curtain dust control in fully mechanized coal mining faces, air curtain dust collection at loading points in tobacco factories, isolation of respiratory infectious diseases in hospitals, air curtain suppression of pollutants in clean rooms, air curtain maintenance of indoor temperatures at commercial building gates, air curtain insulation of refrigerated cabinets and so on. With respect to dust prevention and control, W.R.Reed et al. [1] designed an air curtain shuttle car with a top cover to prevent dust from spreading to the operation room, and the dust control efficiency was 74~83%. Based on CFD-DPM numerical simulation, Wang Hao et al. [2] studied the influence of forced air volume and suction area on air curtain migration and dust suppression in the process of fully mechanized excavation, which can provide a new idea for the study of environmental sustainability in the process of tunnel excavation. The influence of the air volume ratio on dust removal by air curtains in fully mechanized coal mining faces was studied by means of simulation and field experimentation. The results show that the dust removal efficiency in the main working areas reached over 94%. Geng Fan et al. [3] studied the distribution of dust under the action of air curtain isolation in a coal roadway. Cai Peng et al. [4] developed the air curtain dust control technology in a fully mechanized coal mining face; the high-speed air flow field generated at the outlets of two wind turbines formed a triangular air curtain between the shearer and walkway, the dust control rate at each measuring point exceeded 40%, and the dust control rate in the shearer driver's working area exceeded 90%. Xu Huang et al. [5] designed an air curtain dust removal device and proposed a method of air curtain dust removal in the actual heading face. Hao Wang et al. [6] studied the influence of air volume ratio parameters on dust reduction by air curtains in a rock roadway of a fully mechanized coal mining face, established a mathematical model of air flow–dust migration in a fully mechanized coal mining face and verified the correctness of the established model and related parameter settings. Li Xiaochuan et al. [7] designed and optimized the rotating air curtain dust collection system to solve the dust escape problem at the tobacco stem loading point of a tobacco factory, and the dust collection efficiency was as high as 86.93~94.76%. They also developed a cross-flow soft-seal dust control system, which arranged four new air curtain generators in a square to form a plane cross-flow air curtain connected end to end to realize a soft seal. Scholars have also carried out a lot of research on the air curtain theory; taking the small volume cross-flow air curtain generator as the research object, the effects of three structural parameters of the air curtain generator, cross-sectional area, air supply groove and guide vane, on the uniformity, diffusivity and deviation of the air curtain were studied via experiments and FLUENT numerical simulation [8]. Yang-Cheng Shih et al. [9] studied the pollutant diffusion flow field in clean rooms by changing the parameters of air curtain injection velocity, injection angle and installation height, so as to restrain the pollutant diffusion and optimize the sealing performance and improve the sealing efficiency from 0.87 to 0.94. Fu-Yun Zhao et al. [10] studied the effects of jet velocity, air curtain width and shell height on turbulent flow and air curtain sealing performance. Through multivariate linear regression analysis, the detailed relationship between air curtain sealing efficiency and these control parameters was determined. Cao Zhikun et al. [11] proposed an air curtain optimization design strategy for open vertical refrigerated display cabinets based on an air curtain Cooling Loss Two-Fluid (CLTF) model and Support Vector Machine (SVM) algorithm. A model of air curtain cooling loss, which is an important performance factor of display cabinets, is put forward. Wang Haixin et al. [12] proposed a circulating air curtain composed of end-to-end plane jets generated by air column relay to limit exhaled pollutants and explored the partition performance under different conditions, finding better design parameters, e.g., the distance between the human curtain, the shape of closure, the jet velocity of the air column and the exhalation mode. Shu Chang et al. [13] used a series of typical aerodynamic performance curves (for example, $V - \Delta p$) to study an effective method to evaluate the aerodynamic performance of air curtain in terms of reducing permeation/seepage ability. Compared with the existing methods, the new method is more efficient and economical in various air curtain products and installation scenarios. Yang Senwen et al. [14] evaluated the performance of air curtains under different wind velocities of the magnitude and direction through experiments, and the interaction between the air curtain and air curtain jet.

As mentioned above, scholars have carried out detailed research on dust prevention and control based on air curtains and the theory of air curtains. However, there has been little research on the dust suppression of air curtain soft sealing during the unloading process. During the unloading process, the dust diffuses irregularly, which increases the difficulty of dust suppression by air curtain soft sealing. Moreover, previous studies have only focused on the area with a single open cross-section, and the unloading area is an open area, so the intermittent loading and unloading of grab increase the difficulty of research. In this study, the Computational Fluid Dynamics–Discrete Element Method (CFD-DEM) coupling method was used, and the diffusion law of the gas–solid two-phase flow field of the falling bulk material was studied, and the motion trajectory and velocity distribution of the particle flow field and air flow field were obtained, as well as the maximum air flow field velocity of five planes above the hopper. The maximum air flow field velocity was selected as the boundary condition, and the air curtain and air flow field model were constructed using Fluent software. By comparing the barrier performance of air curtains (under different design parameters), the optimal design parameters for air curtains were obtained.

2. Numerical Simulation and Law Study of Gas–Solid Two-Phase Flow Field in Grab Unloading

2.1. Simulation Method

For the numerical simulation and law research of gas–solid two-phase flow of grab unloading, the CFD-DEM coupling method was used, and the Eulerian–Lagrangian model was adopted, the fluid phase is described by the continuous method under the Eulerian framework, and the solid phase is described by the discrete method under the Lagrangian framework. The basic model is was as follows: a complete discrete element solver was used to calculate particles, which occupied the fluid volume and interacted with the fluid. According to the governing equations of CFD-DEM coupling and the equations of the fluid–particle interaction force, the basic theory of the CFD-DEM governing equations and the fluid–particle interaction forces are as follows.

2.1.1. CFD-DEM Governing Equations

The gas-phase continuity equation in gas–solid two-phase flow is given as:

$$\frac{\partial}{\partial t}\left(\alpha_g \rho_g\right) + \nabla \cdot \left(\alpha_g \rho_g u_g\right) = 0 \tag{1}$$

The momentum conservation equation is given as:

$$\begin{aligned} &\tfrac{\partial}{\partial t}\left(\alpha_g \rho_g u_g\right) + \nabla \cdot \left(\alpha_g \rho_g u_g u_g\right) \\ &= -\alpha_g \nabla p + \nabla \cdot \left(\alpha_g \tau_g\right) + \alpha_g \rho_g g - F_{g-p} \end{aligned} \tag{2}$$

where α_g, ρ_g, u_g and p are the volume fraction, density, velocity and pressure of the gas, respectively, τ_g denotes the viscous stress tensor of gas and g the gravitational acceleration, and F_{g-p} is the force between the particle phase and gas phase.

In the Euler–Lagrangian method, each particle of the solid phase is solved individually, so as to obtain detailed particle motion dynamics information, including particle–particle, particle–gas and particle–wall interactions. According to Newton's second law, the motion equation of the solid phase is given as:

$$m_i \frac{\mathrm{d}v_i}{dt} = m_i g + f_{p-g,i} + \sum_{j=1}^{k_i} f_{contact,ij} \tag{3}$$

$$I_i \frac{\mathrm{d}\vec{w}_i}{dt} = \sum_{j=1}^{k_i} \vec{T}_{ij} \tag{4}$$

where m_i, I_i, $\vec{v}_i$ and $\vec{w}_i$ are the mass, moment of inertia, translational velocity and angular velocity of particle i, respectively. k_i is the number of particles in contact with particle i, T_{ij} is torque, and $f_{p-g,i}$ and $f_{contact,ij}$ are the gas–solid interaction force and contact force of particles, respectively.

2.1.2. Fluid–Particle Interaction Forces

According to the empirical correlations for pressure drop, the particle–fluid drag force can be represented by the interphase momentum transfer coefficient and the slip velocity, which are given by:

$$F_d = \frac{\beta(u_g - u_p)}{\rho_g} \tag{5}$$

where u_g and u_p are the velocity of gas and particles, respectively. β is the interphase momentum transfer coefficient. A proper drag model for the description of β is vital in CFD-DEM simulation. A combination of the Ergun and the Wen Yu correlations is often used. β is given by:

$$\beta = \begin{cases} 150\frac{\left(1-\varepsilon_g\right)^2 \mu_g}{\varepsilon_g d_p^2} + 1.75\frac{\left(1-\varepsilon_g\right)\rho_g}{d_p}\left|u_g - u_p\right|, \varepsilon_g \le 0.8 \\ \frac{3}{4} C_D \frac{\left(1-\varepsilon_g\right)\rho_g}{d_p}\left|u_g - u_p\right| \varepsilon_g^{-2.65}, \varepsilon_g > 0.8 \end{cases}, \tag{6}$$

where μ_g, d_p and C_D are the gas viscosity, particle diameter and drag coefficient, respectively. The drag coefficient C_D is written as:

$$\mathrm{C}_D = \begin{cases} \frac{24}{Re}\left(1 + 0.15 Re^{0.687}\right), Re \le 1000 \\ 0.44, Re > 1000 \end{cases} \tag{7}$$

where Re is given by:

$$Re = \frac{\varepsilon_g \rho_g d_p \left|u_g - u_p\right|}{\mu_g} \tag{8}$$

The gas pressure gradient force is given by:

$$F_p = V_p \nabla_p, \tag{9}$$

where V_p and ∇_p are the particle volume and the gas pressure, respectively.

2.2. Simulation Modeling

To obtain the motion trajectory and velocity distribution of the particle flow field and air flow field, the movement and diffusion of dust must be qualitatively reflected. Firstly, the CFD-DEM coupling method was used to obtain the diffusion law of the air flow field. Then, according to the material characteristics of the dust, the corresponding suspension velocity was obtained, because dust has a strong follow-up in the air flow field, combined with the motion trajectory and velocity distribution of the air flow field, and the movement and diffusion of dust were finally obtained.

As shown in Figure 2, a three-dimensional model of a rectangular hopper and grab was established and imported into EDEM. As shown in Figure 3, a three-dimensional model of fluid was established, and a fluid area model of unloading was imported into Fluent; the fluid area included grab, particle flow falling and hopper area. The relative coordinates of the fluid domain model and a three-dimensional model were consistent. The fixed time step was 1×10^{-4} s, and the number of time steps was 30,000; that is, the simulation time was 3 s. We selected a hexahedral grid with a side length of 100~200 mm for grid division. The hexahedral grid with a side length of 100~200 mm was selected for mesh generation.

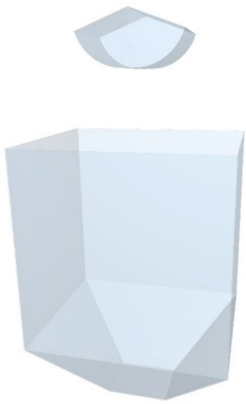

Figure 2. Cuboid hopper and grab model.

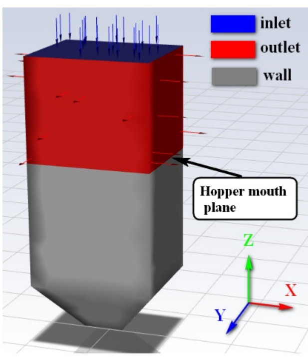

Figure 3. Three-dimensional model of the fluid domain.

The three-dimensional model of the grab unloading was imported into EDEM, and the parameter settings are shown in Table 1. We set the fluid boundary conditions and parameters, as shown in Table 2.

Table 1. DEM parameters used in simulations.

Parameters	Values	Parameters	Values
Particle diameter (mm)	5, 10, 30	Geometric shear modulus (Pa)	7.9×10^{10}
Total mass of particles (kg)	220	Particle–particle restitution coefficient	0.5
Particle Poisson ratio	0.4	Particle–particle static friction coefficient	0.6
Particle density (kg/m^3)	1023	Particle–particle rolling friction coefficient	0.04
Particle shear modulus (Pa)	1.1×10^7	Particle–geometry restitution coefficient	0.5
Geometric Poisson ratio	0.3	Particle–geometry static friction coefficient	0.4
Geometric density (kg/m^3)	7850	Particle–geometry rolling friction coefficient	0.05

Table 2. CFD model description.

Description	Model
Solver	Pressure-based
Viscous model	Standard k-epsilon
Inlet	Pressure inlet (gauge pressure = 0)
Outlet	Pressure outlet (gauge pressure = 0)
Wall	Stationary wall (no slip)

2.3. Motion Trajectory and Velocity Distribution of Particle Flow Field and Air Flow Field

According to the basic theory of CFD-DEM governing equations and fluid–particle interaction forces, the motion trajectory and velocity distribution of the particle flow field and air flow field were analyzed. The results show that the particles interacted with the surrounding air during the unloading process; particle flow drove the air to form induced air flow, and, at the same time, induced air flow entrained fine particles in the particle flow to form a dust-laden air flow, resulting in dust overflow. The highest velocities of the particle flow field and air flow field were 10.14 m/s and 2.24 m/s, respectively.

As shown in Figure 4, the motion trajectories and velocity distributions of the particle flow field and air flow field at t = 0.8 s, 1.6 s and 2.4 s correspond to the free-falling stage, the material accumulation stage and the flow field attenuation stage, respectively. The three stages are described in detail as follows.

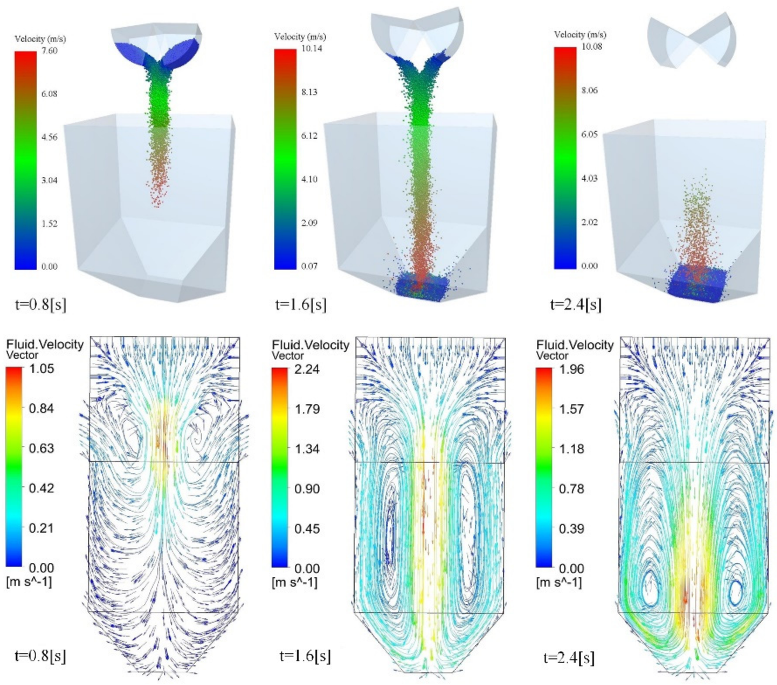

Figure 4. Motion trajectory and velocity distribution of particle flow field and air flow field.

The free-falling stage: Part of the particle flow field entered the hopper, which increased the disturbance of the air flow field. The particle flow edge near the induced air velocity changed significantly, and the air flow shearing effect in this area was obvious. As can be seen in the velocity streamline diagram of the air flow field, the induced air moved downward with the falling of the particle flow, and the direction was nearly parallel to the vertical direction, the diffusion in the horizontal direction was weak, and a small vortex was formed above the hopper mouth.

The material accumulation stage: The particle flow continued to fall, which strengthened the disturbance of the air flow field. At this stage, the particle flow had an obvious effect on the air flow field, and the shearing effect of downward moving air flow was strengthened, so that the positive pressure inside the hopper increased rapidly, and the air flow field formed a vortex in the hopper, carrying escaping dust above the hopper, and the amount of escaping dust reached the maximum.

The flow field attenuation stage: Most of the particle flow field accumulated at the bottom of the hopper, and the particles collided with each other, and the particle flow field collided with the hopper wall, causing secondary dust. At this time, the velocity of the air flow field decreased, and the amount of dust escaping decreased.

2.4. Analysis of Air Flow Field in Five Planes above the Hopper

As shown in Figure 5, the gray shadow is a schematic diagram of five planes above the hopper, which cover the grab bucket in the hopper. The changes in the maximum air flow velocity and the average air flow velocity of five planes above the hopper over time during the grab unloading process were analyzed.

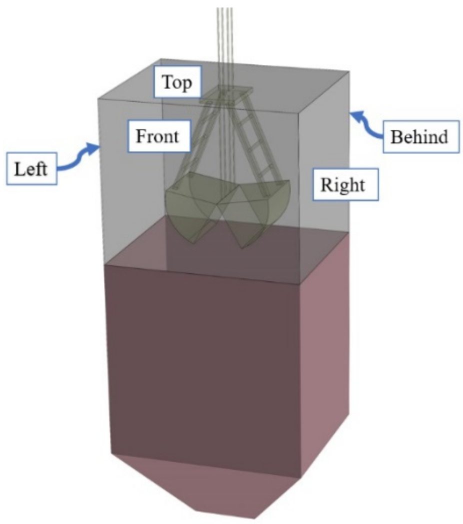

Figure 5. Schematic diagram of five planes above the hopper.

As shown in Figure 6, the average and maximum air flow field velocities of five planes above the hopper during the unloading process were calculated. The results show that the velocity of the air flow field in each plane increased first and then decreased with time, and the velocity curves of the opposite plane had the same trend. Furthermore, the values of each point were similar. The average and maximum air flow field velocity of each plane descended in the following order: left side and right side, front side and back side, top side. The air flow field velocities of the top side were far less than that those of the four sides, and the air flow field velocities of the four sides were close. The maximum air flow field velocities at the top side and the four sides were 0.161 m/s and 0.778 m/s, respectively.

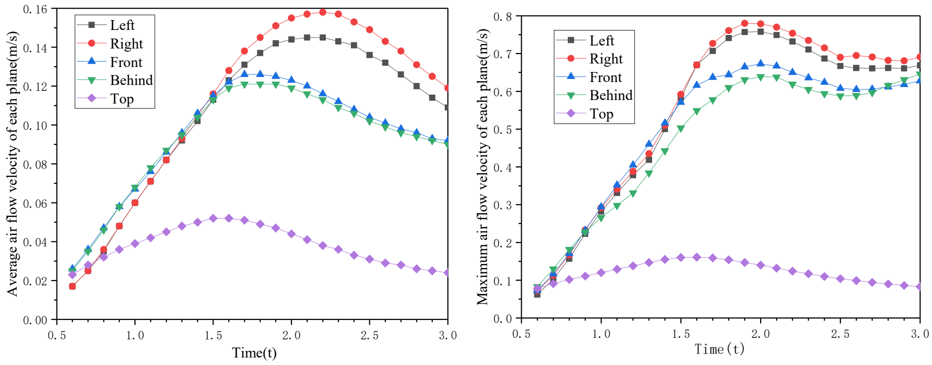

Figure 6. Velocity of air flow field in each plane during unloading process: (**a**) average velocity; (**b**) maximum velocity.

When the particle density was 1023 kg/m^3 and the air flow field velocity was 0.161 m/s, the corresponding suspended particle size was 70 µm. Therefore, dust with a particle size above 70 µm did not escape, so the dust diffusion on the top plane can be ignored, and dust escaping from four sides was mainly considered [15].

3. Numerical Simulation of Barrier Performance of Air Curtain

In Section 2, the numerical simulation of the gas–solid two-phase flow field of grab unloading was carried out, and the motion trajectory and velocity distribution of the particle flow field and the air flow field were obtained, as well as the maximum air flow field velocity and average air flow field velocity of five planes above the hopper. Since the velocity of the air flow field on the top side was far less than that on the four sides, the dust diffusion on the top plane can be ignored, and the air curtain was designed to block the four sides, and the air curtain parameters were set based on the maximum air flow field velocity, and a simplified three-dimensional model of air curtain jet was constructed using Fluent software to analyze the barrier performance of the air curtain.

3.1. Simulation Modeling of Air Curtain and Air Flow Field

As shown in Figure 7, the arrows show the direction of the air curtain jet, and the four air curtain jet planes above the hopper formed a closed air curtain. Considering the complexity of the air flow field during the unloading process, that is, the magnitude and direction of velocity of the air flow field at different positions changed constantly, the simulation model was simplified, and the air curtain parameters were set based on the maximum velocity of the air flow field, and the velocity direction remained unchanged.

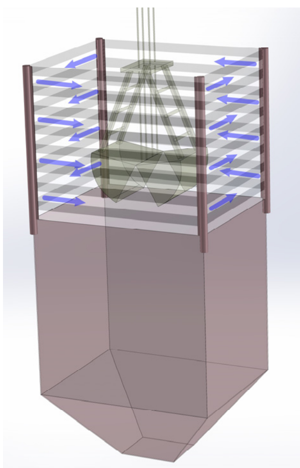

Figure 7. Schematic diagram of air curtain soft-sealing system.

As shown in Figure 8, the three-dimensional model of the fluid region was composed of four air columns and a cylinder. The cylinder was located in the center of the air column, ignoring the fluid region of the lower hopper, and only considering the interaction between the air curtain and the dust carried by the induced wind. The side of the cylinder was the outlet plane of induced wind, and the velocity was 0.778 m/s (calculated according to 0.8 m/s for the convenience of simulation and comparison). Four air column jets formed a clockwise air curtain, and the arrows in the top view represent the direction of air curtain jet and air flow field.

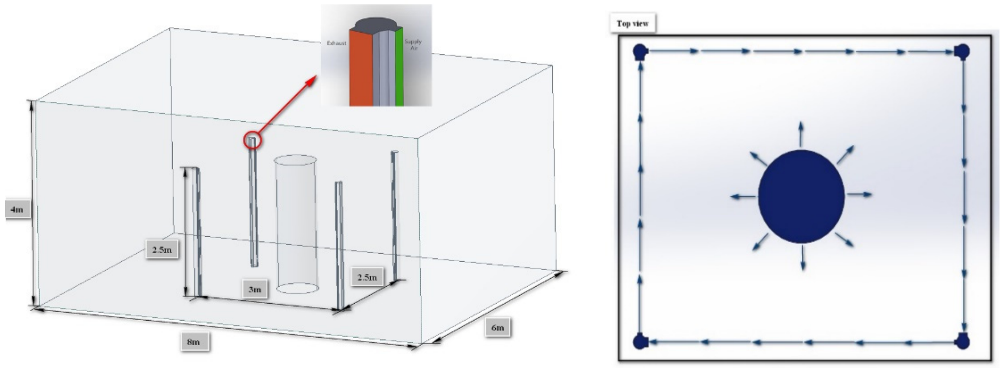

Figure 8. Three-dimensional model of the fluid region.

The size of the fluid domain was 8 m (length) × 6 m (width) × 4 m (height), the diameter of the cylinder was 0.8 m, the height was 2.5 m, the distance between the air columns was 3 m × 2.5 m, and the height was 2.5 m.

3.2. CFD Parameter Settings

Computational fluid dynamics (CFD) is the study of the interaction between air curtains and pollutants. In Fluent 18.0, the SIMPLE algorithm and Second Order Upwind scheme were used to solve the governing equations of fluid flow. A standard k-ε turbulence model was used, and the no-slip boundary condition was used as a boundary condition.

The vector form of the governing equations is expressed as follows:

$$\frac{\partial \rho}{\partial t} + \mathrm{div}(V) = 0 \tag{10}$$

$$\frac{\partial(\rho\phi)}{\partial t} + \mathrm{div}(\rho V \phi) = \mathrm{div}(\Gamma_\phi \mathrm{grad}\phi) + S_\phi \tag{11}$$

where V is the velocity vector, ϕ is a general scalar quantity, which can represent three components of velocity, kinetic energy of turbulence k, the dissipation rate of turbulence energy ε, temperature T and tracer gas concentration. ρ is the fluid density, Γ_ϕ is the diffusion term, and S_ϕ is the source term.

The Species Transport Model and N_2 were selected in the species as the tracer gas to track the diffusion range and concentration distribution of pollutants, with an initial mass fraction of 10%.

The Discrete Phase Model (DPM) was implemented to simulate the diffusion of dust particles. The trajectory of dust particles was predicted by solving the following equations:

$$\frac{\mathrm{d}\vec{u}_p}{dt} = F_D(\vec{u} - \vec{u}_p) + \frac{\vec{g}(\rho_p - \rho)}{\rho_p} + \vec{F} \tag{12}$$

$$F_D = \frac{18\mu}{\rho_p d_p^2} \frac{C_D Re}{24} \tag{13}$$

$$Re \equiv \frac{\rho d_p \left| \vec{u}_p - \vec{u} \right|}{\mu} \tag{14}$$

where d_p is the particle diameter, C_D is the drag coefficient, $\vec{F}$ is the additional acceleration (force/unit particle mass) term, g is the gravity acceleration, $\vec{u}$ is the fluid phase velocity, $\vec{u}_p$ is the particle velocity, μ is the fluid molecular viscosity, Re is the relative Reynolds number, ρ is the fluid density and ρ_p is the particle density.

In the DPM, the particle size of dust was 20 µm, which is a normal distribution, and the dust was released from the side of the cylinder. Only gravity, drag force and buoyancy were considered, and other forces were ignored.

3.3. Grid Independence Test

As shown in Figure 9, taking case 1 as the grid independence test, three different types of grids were generated, with the amount of 210,370, 429,612 and 600,424. The three grids all satisfied the minimum orthogonal quality, being greater than 0.1, the maximum skewness was less than 0.95, the quality of the grids satisfied the requirements, the horizontal velocities of grid 1, grid 2 and grid 3 were compared, the structures of the three grids were similar, and the average deviation between grid 1 and grid 3 along the three lines was 8.6%, The discrepancies between the three mesh systems were acceptable. Therefore, considering the calculation accuracy and time, grid 1 was selected for analysis.

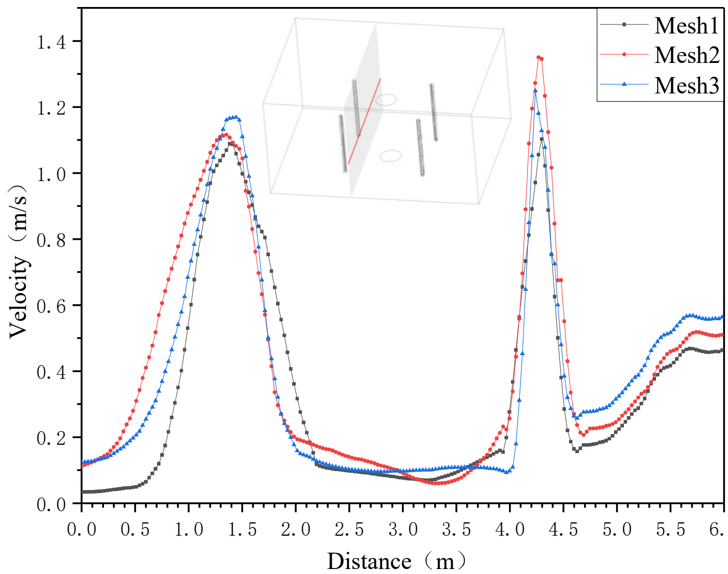

Figure 9. Comparison of horizontal velocities of different grids.

3.4. Design of Air Curtain Parameters

Table 3 shows the simulation cases under different air curtain parameters, using the control variable method. The variables were air curtain jet modes (blow and suction, unilateral blowing, bilateral blowing), jet widths (10 mm, 20 mm, 40 mm), jet velocities (3.5 m/s, 5.0 m/s, 6.5 m/s) and induced wind velocities (0.5 m/s, 0.8 m/s, 1.1 m/s). Each case is marked as case # (air curtain jet mode; jet width; jet velocity; induced wind velocity). For example, case 1 is referred to as (blow and suction; 20 mm; 5.0 m/s; 0.8 m/s). In order to obtain better design parameters for air curtains, distributions of velocity vectors and the diffusion range of pollutants were studied.

Table 3. Simulation cases under different air curtain parameters.

Scenario	Case	Air curtain Jet Mode	Jet Width (mm)	Jet Velocity(m/s)	Induced Wind Velocity(m/s)
1	1	blow and suction	20	5	0.8
	2	blow and suction	10	5	0.8
	3	blow and suction	40	5	0.8
2	1	blow and suction	20	5	0.8
	4	unilateral blowing	20	5	0.8
	5	bilateral blowing	20	2.5	0.8
3	1	blow and suction	20	5	0.8
	6	blow and suction	20	3.5	0.8
	7	blow and suction	20	6.5	0.8
4	1	blow and suction	20	5	0.8
	8	blow and suction	20	5	1.1
	9	blow and suction	20	5	0.5

4. Experiment and Validation

An air curtain soft-sealing system was designed to measure the dust concentration outside the air curtain, as shown in Figure 10. The system was mainly composed of air columns, an induced wind device, dust-rising device and dust-measuring device. The air columns and the induced wind device were fed by two blowers connected to the hose, and the air supply volume was adjusted to the specified test value. The induced wind device drove a dust-raising device to continuously form dust flow in the air curtain.

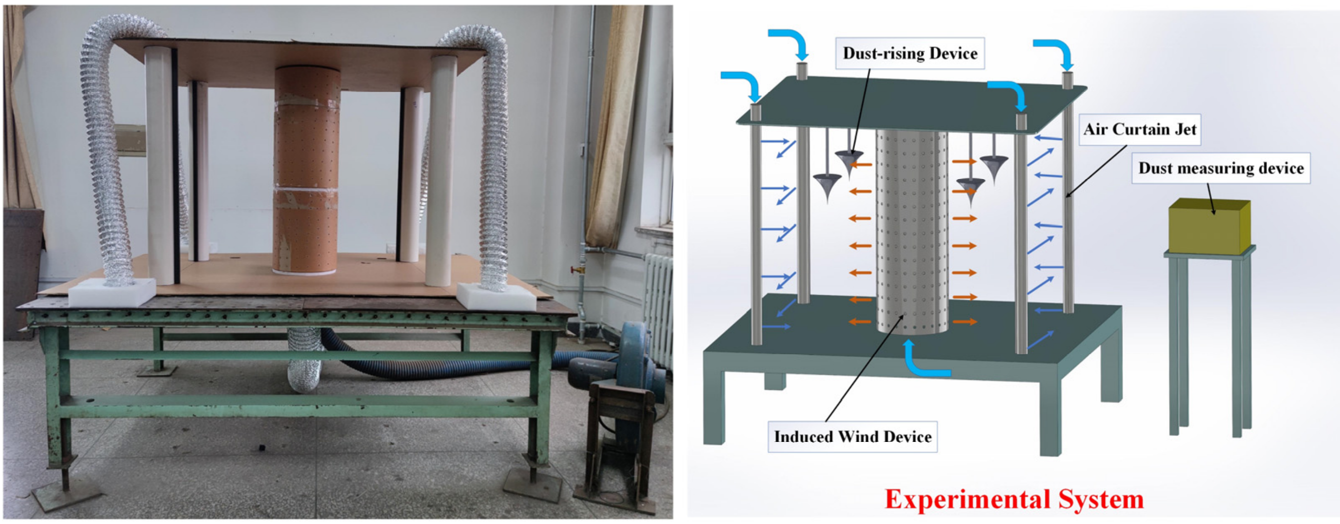

Figure 10. The experimental test of air curtain soft-sealing system.

In order to verify the accuracy of the numerical settings, experiments were carried out with the parameters of case 1 using the dust-measuring device, which had an error of 15% and a precision of 0.1 mg/m^3, as shown in Figure 11. The dusty air flow was suctioned into the dust-measuring device at a rate of 7.2 L/min, the dust concentration of which was measured based on the principle of the light-scattering method. The dust concentration was determined by measuring the intensity of scattered light.

Figure 11. Dust-measuring device.

A total of six data points were selected from 1.75 m to 3 m in the horizontal direction of the cylindrical axis. Each data point was measured three times, and the result is the average value of the three experiments. Figure 12 shows the comparison of concentrations in experimental and numerical results. It can be seen that the experimental results are consistent with the numerical simulation results. The C/C_0 ratio in the experiment was slightly larger than in the numerical simulation, but within the error range. The results are reasonable, and the numerical set-up can be validated as reliable.

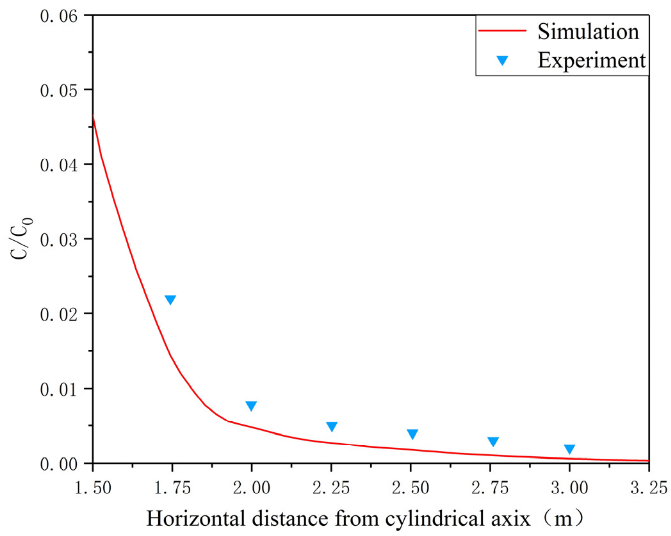

Figure 12. Comparison of dust concentration between simulation and experiment.

5. Analysis and Discussion of Barrier Performance of Air Curtain

5.1. Distributions of Velocity Vectors and Diffusion Range of Pollutants

Figures 13 and 14 show distributions of the velocity vector diagram and the diffusion range of pollutants in the cloud diagram at the height y = 1.5 m of the model under different air curtain parameters. The air curtain jet formed a closed loop to block the pollutants, and the velocity gradually decreased from the inlet to the opposite side.

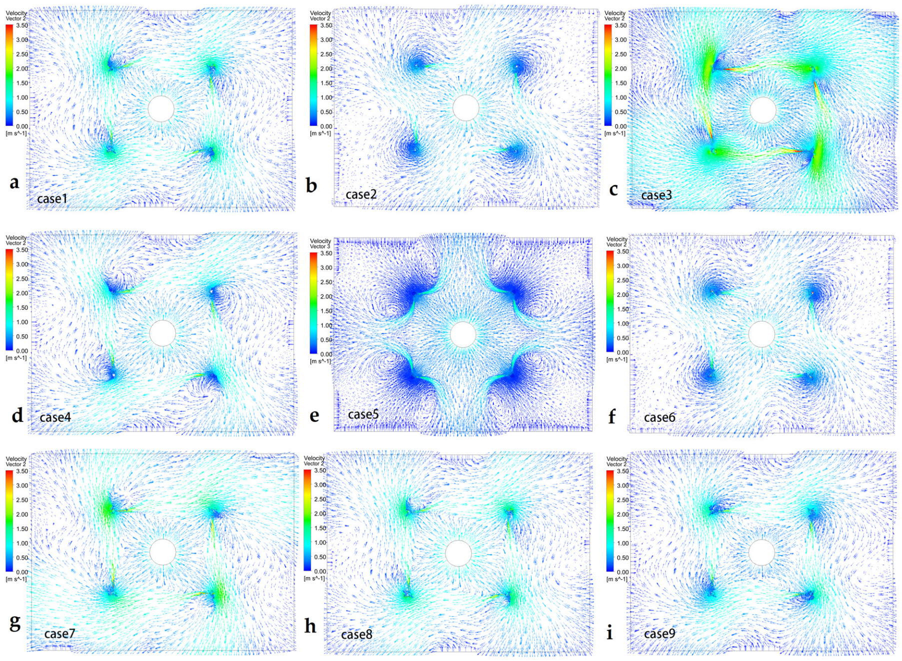

Figure 13. Distributions of velocity vectors under various air curtain parameters: (**a**) case 1 (blow and suction; 20 mm; 5 m/s; 0.8 m/s); (**b**) case 2 (blow and suction; 10 mm; 5 m/s; 0.8 m/s); (**c**) case 3 (blow and suction; 40 mm; 5 m/s; 0.8 m/s); (**d**) case 4 (unilateral blowing; 20 mm; 5 m/s; 0.8 m/s); (**e**) case 5 (bilateral blowing; 20 mm; 5 m/s; 0.8 m/s); (**f**) case 6 (blow and suction; 20 mm; 3.5 m/s; 0.8 m/s); (**g**) case 7 (blow and suction; 20 mm; 6.5 m/s; 0.8 m/s); (**h**) case 8 (blow and suction; 20 mm; 5 m/s; 1.1 m/s); (**i**) case 9 (blow and suction; 20 mm; 5 m/s; 0.5 m/s).

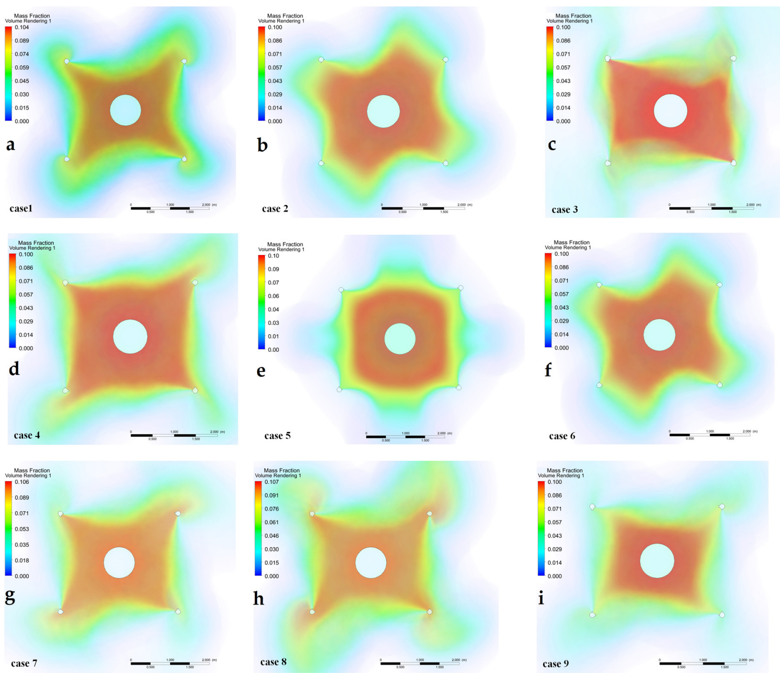

Figure 14. The pollutants' mass fraction under various air curtain parameters: (**a**) case 1 (blow and suction; 20 mm; 5 m/s; 0.8 m/s); (**b**) case 2 (blow and suction; 10 mm; 5 m/s; 0.8 m/s); (**c**) case 3 (blow and suction; 40 mm; 5 m/s; 0.8 m/s); (**d**) case 4 (unilateral blowing; 20 mm; 5 m/s; 0.8 m/s); (**e**) case 5 (bilateral blowing; 20 mm; 5 m/s; 0.8 m/s); (**f**) case 6 (blow and suction; 20 mm; 3.5 m/s; 0.8 m/s); (**g**) case 7 (blow and suction; 20 mm; 6.5 m/s; 0.8 m/s); (**h**) case 8 (blow and suction; 20 mm; 5 m/s; 1.1 m/s); (**i**) case 9 (blow and suction; 20 mm; 5 m/s; 0.5 m/s).

Figures 13a–c and 14a–c show that the jet width varied from 20 mm to 10 mm to 40 mm; the smaller the jet width, the more obvious the deflection of the air curtain and the weaker the overall pollutant restriction. However, when the jet width was 40 mm, pollutants diffused obviously on the opposite side of the air curtain jet.

Figure 13a,d,e and Figure 14a,d,e show that different air curtain jet modes (blow and suction, unilateral blowing, bilateral blowing) were changed, unilateral blowing could not effectively form a closed loop because there was no suction port on the opposite side, and pollutants were diffused on the opposite side. Under the coupling action of the pollutant and air curtain, the bilateral blowing easily converged, and unstable turbulent diffusion was formed at the intersection, which led to the diffusion of pollutants and a poor barrier effect.

Figure 13a,f,g and Figure 14a,f,g show that the jet velocity varied from 5 m/s to 3.5 m/s to 6.5 m/s; the higher the jet velocity, the stronger the entrainment effect of the air curtain, the smaller the deflection of the air curtain and the weaker the overall pollutant restriction. However, when the jet velocity was 6.5 m/s, the pollutants diffused obviously on the opposite side of the air curtain jet.

Figure 13a,h,i and Figure 14a,h,i show that when the induced wind velocity varied from 0.8 m/s to 1.1 m/s to 0.5 m/s, the air flow velocity was proportional to the instantaneous unloading, and the change in air flow field velocity had a slight influence on the air curtain barrier effect.

5.2. The Variation in the Mass Fraction of Pollutants in the Horizontal Direction

In order to quantify the performance of air curtains in limiting pollutants, the length of the air curtain jet was set as 2.5 m, and the distance between the air curtain and the cylindrical axis was set as 1.5 m, and the concentration of pollutants was varied with the horizontal distance from the cylindrical axis, as shown in Figure 12, and the non-air curtain jet was taken as the reference, compared with the air curtain barrier performance of different jet widths (10 mm, 20 mm, 40 mm), different air curtain jet modes (blow and suction, unilateral blowing, bilateral blowing) and different jet velocities (3.5 m/s, 5.0 m/s, 6.5 m/s). In addition, the effects of different induced wind velocities (0.5 m/s, 0.8 m/s, 1.1 m/s) on the air curtain barrier performance were compared, and the device's applicability was verified.

Figure 15a, which depicts the horizontal variations in pollutants with different jet widths (10 mm, 20 mm, 40 mm) and the non-air curtain jet, reveals that the rapid decline in the pollutant mass fraction mainly occurred at 1.4~2.0 m. Compared with the non-air curtain jet, when the air curtain jet width was 10 mm, the mass fraction of pollutants outside the air curtain did not decrease significantly, which indicates that the air curtain with this width did not limit the pollutants in the air curtain and hardly formed a barrier. When the jet widths were 20 mm and 40 mm, the descending slope of the pollutant mass fraction in the air curtain jet plane increased, and it remained low (0.01) and stable after 2.0 m, which indicates that the air curtain with this width could confine pollutants within the air curtain and effectively prevent pollutants from spreading outward. The air curtain with a width of 20 mm was better than the air curtain with a width of 40 mm, because a large number of pollutants were swallowed when the jet width was large, which expanded the influence range and led to a certain degree of diffusion of pollutants outside the air curtain. The average mass fraction of pollutants outside the air curtain at jet widths of 20 mm, 10 mm and 40 mm was 0.006604, 0.019007 and 0.0166617. The order of the barrier effect of the air curtain studied was 20 mm, 40 mm and 10 mm. Selecting the appropriate jet width could reduce the spread of pollutants.

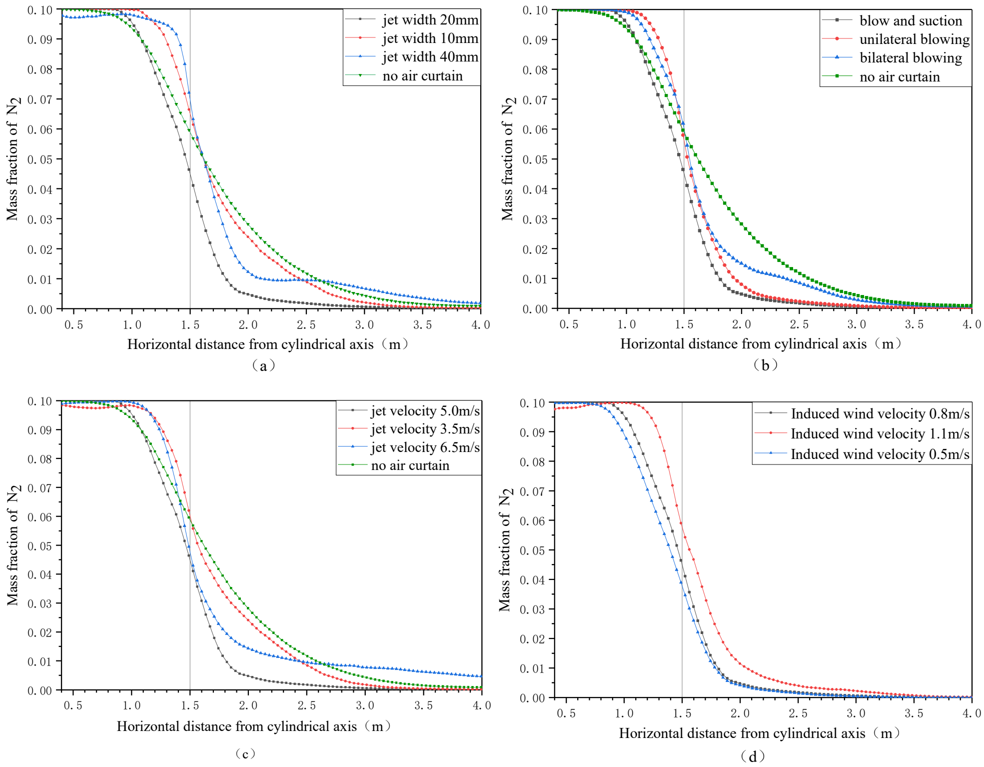

Figure 15. The pollutants' mass fraction at the horizontal distance from the cylindrical axis: (**a**) jet width (blow and suction; 20 mm–10 mm–40 mm; 5 m/s; 0.8 m/s); (**b**) air curtain jet mode (blow and suction, unilateral blowing, bilateral blowing; 20 mm; 5 m/s; 0.8 m/s); (**c**) jet velocity (blow and suction; 20 mm; 5 m/s–3.5 m/s–6.5 m/s; 0.8 m/s); (**d**) induced wind velocity (blow and suction; 20 mm; 5.0 m/s; 0.8 m/s–1.1 m/s–0.5 m/s).

Figure 15b, which depicts the horizontal variations in pollutants with different jet modes (blow and suction, unilateral blowing, bilateral blowing) and the non-air curtain jet reveals that the rapid decline in the pollutant mass fraction mainly occurred at 1.3–1.8 m. Compared with the non-air curtain jet, under the three air curtain jet modes, the mass fraction of pollutants outside the air curtain jet plane decreased significantly, and the blocking effect was obvious. The average mass fractions of pollutants outside the air curtain at different jet modes (blow and suction, unilateral blowing, bilateral blowing) were 0.006604, 0.009459 and 0.014355. The order of the barrier effect of the air curtain studied was blow and suction, unilateral blowing and bilateral blowing. Selecting the appropriate jet modes could reduce the spread of pollutants.

Figure 15c, which depicts the horizontal variations in pollutants with different jet velocities (3.5 m/s, 5.0 m/s, 6.5 m/s) and the non-air curtain jet reveals that the rapid decline in the pollutant mass fraction mainly occurred at 1.1~1.8 m. Compared with the non-air curtain jet, when the air curtain jet velocity was 3.5 m/s, the mass fraction of pollutants outside the air curtain did not decrease significantly, indicating that the air curtain at this velocity did not confine the pollutants, and hardly formed a barrier. When the jet velocity was 5.0 m/s and 6.5 m/s, the decreasing slope of the pollutants' mass fraction at the plane position of the air curtain jet increased, and the blocking effect was obvious. Moreover, the mass fraction remained low (0.014) at 2.0 m, and remained stable during the entire course of the experiment. This shows that the air curtain jet could confine the pollutants and effectively prevent the pollutants from spreading outward. The air curtain with a jet velocity of 5.0 m/s had a better barrier effect than the air curtain with a jet velocity of 6.5 m/s, because a large number of pollutants were swallowed up when the jet velocity was high, which expanded the influence range and led to a certain degree of diffusion of pollutants outside the air curtain. The average mass fraction of pollutants outside the air curtain with the jet velocities of 3.5 m/s, 5.0 m/s and 6.5 m/s were 0.018330, 0.006604 and 0.014507. The order of the barrier effect of the air curtain studied was 5.0 m/s, 6.5 m/s and 3.5 m/s. Selecting the appropriate jet velocity could reduce the spread of pollutants.

Figure 15d, which depicts the horizontal variations in pollutants with different induced wind velocities (0.5 m/s, 0.8 m/s, 1.1 m/s), shows that the average mass fractions of pollutants outside the air curtain with induced wind velocities of 0.5 m/s, 0.8 m/s and 1.1 m/s were 0.005719, 0.006604 and 0.012605. The order of the barrier effect of the air curtain studied was 0.5 m/s, 0.8 m/s and 1.1 m/s. When the induced wind velocities were 0.5 m/s and 0.8 m/s, the mass fraction of pollutants outside the air curtain did not change significantly; in contrast, when the induced wind velocity was 1.1 m/s, the mass fraction of pollutants increased slightly, but it was also within the controllable range. The results show that under a certain range of induced wind velocity values, the air curtain had a certain restricting effect on the diffusion of pollutants.

As determined from the above analysis, the better air curtain design parameters were as follows: jet mode, blow and suction, jet width, 20 mm and jet velocity, 5 m/s. Compared with the non-air curtain jet, the average mass fraction of pollutants outside the air curtain decreased by 70.02%.

Compared with the non-air curtain jet, statistical data for pollutants outside the air curtain under different air curtain cases are shown in Table 4.

Table 4. Statistical data for pollutants outside the air curtain under different air curtain cases.

Case	The Average Mass Fraction of Pollutants outside the Air Curtain	Compared with the Non-Air Curtain Jet, the Average Mass Fraction of Pollutants outside the Air Curtain Decreased (%)
1	0.006604	70.02
2	0.019007	13.71
3	0.016662	24.36
4	0.009459	57.06
5	0.014355	34.83
6	0.018330	16.78
7	0.014507	34.14
8	0.005719	74.03
9	0.012605	42.78

Figure 16 shows the superposition diagram of the velocity vector and the pollutants' mass fraction in the transient simulation of case 1. At 0~5 s, the closed-loop process of the air curtain jet was formed; at 5~10 s, the pollutants began to diffuse and the air curtain was formed, and the jet confined the contaminants within the air curtain.

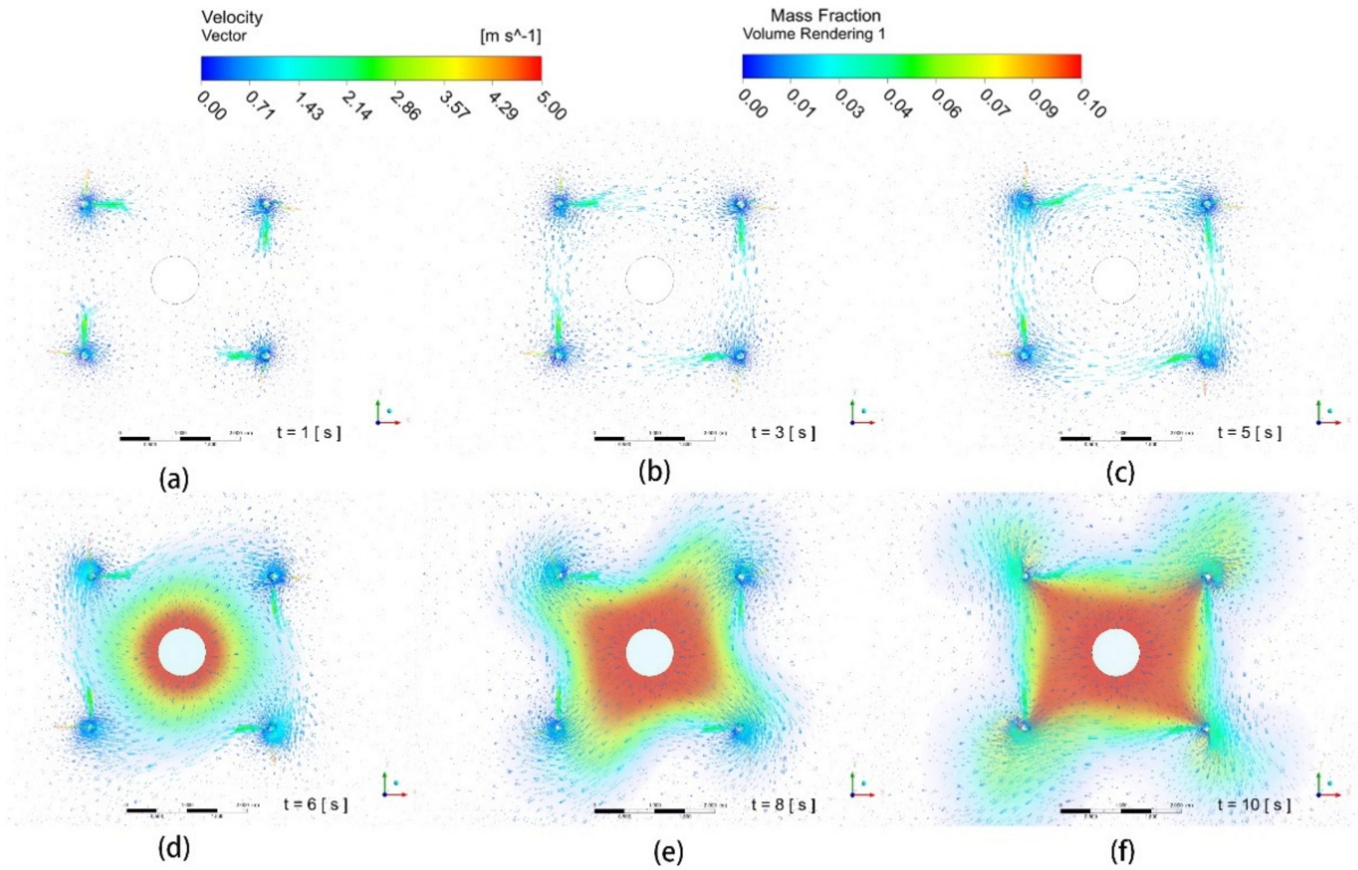

Figure 16. The superposition diagram of velocity vector and pollutant mass fraction in transient simulation of case 1: (**a**) time = 1 s; (**b**) time = 3 s; (**c**) time = 5 s; (**d**) time = 6 s; (**e**) time = 8 s; (**f**) time = 10 s.

6. Conclusions

In this paper, law research of gas–solid two-phase flow field in grab unloading was carried out, and the motion trajectory and velocity distribution of the particle flow field and air flow field were obtained, so as to design an air curtain soft-sealing system which can effectively block the air flow and restrict the diffusion of pollutants. The results show that the average mass fraction of pollutants outside the air curtain plane decreased by 13.71~74.03% under different air curtain parameters. The order of the barrier effect of the air curtain jet width was 20 mm, 40 mm and10 mm, and the order of the barrier effect of the air curtain jet velocity was 5.0 m/s, 6.5 m/s and 3.5 m/s. Selecting the appropriate jet width and jet velocity could significantly reduce the pollutants' diffusion; under different jet modes, the order of the barrier effect of the air curtain jet modes were blow and suction, unilateral blowing and bilateral blowing. In addition, under a certain range of induced wind velocities, the air curtain had a certain restricting effect on the diffusion of pollutants. In general, the air curtain could effectively block the irregular diffusion of dust during the unloading process. In this work, the air curtain device could be conveniently applied to material transfer places such as ports, thermal power plants and granaries. It deserves further research and development.

However, this subject remains to be further studied. First, the corresponding relationship between dust production from grab unloading with different specifications and air curtain parameters was studied to meet the dust suppression effect of the air curtain with different specifications. Second, in the unloading process, the variation in dust production and air curtain parameters at different times was studied to improve dust suppression efficiency and reduce energy consumption.

Author Contributions: Conceptualization, H.Z. and W.M.; methodology, H.Z.; software, H.Z.; validation, H.Z. and W.M.; formal analysis, H.Z.; investigation, H.Z.; resources, W.M.; data curation, H.Z.; writing—original draft preparation, H.Z.; writing—review and editing, W.M.; visualization, H.Z.; supervision, H.Z.; project administration, W.M.; funding acquisition, W.M. All authors have read and agreed to the published version of the manuscript.

Funding: This research was funded by the National Natural Science Foundation of China, grant number 52075356.

Institutional Review Board Statement: Not applicable.

Informed Consent Statement: Not applicable.

Data Availability Statement: The study did not report any data.

Conflicts of Interest: The authors declare no conflict of interest.

References

1. Reed, W.R.; Zheng, Y.; Yekich, M. Laboratory testing of a shuttle car canopy air curtain for respirable coal mine dust control. *Int. J. Coal Sci. Technol.* **2018**, *5*, 10. [CrossRef]
2. Wang, H.; Sa, Z.; Cheng, W. Effects of forced-air volume and suction region on the migration and dust suppression of air curtain during fully mechanized tunneling process. *Process. Saf. Environ. Prot.* **2020**, *145*, 222–235. [CrossRef]
3. Geng, F.; Gui, C.; Wang, Y.; Zhou, F.; Hu, S.; Luo, G. Dust distribution and control in a coal roadway driven by an air curtain system: A numerical study. *Process. Saf. Environ. Prot.* **2019**, *121*, 32–42. [CrossRef]
4. Cai, P.; Nie, W.; Liu, Z. Study on the air curtain dust control technology with a dust purifying fan for fully mechanized mining face. *Powder Technol.* **2020**, *374*, 507–521. [CrossRef]
5. Huang, X. Air Curtain Dust Removal Device Design and Dust Prevention Strategy in Heading Face. *Adv. Civ. Eng.* **2020**, *2020*, 8891599. [CrossRef]
6. Wang, H.; Nie, W.; Cheng, W. Effects of air volume ratio parameters on air curtain dust suppression in a rock tunnel's fully-mechanized working face. *Adv. Powder Technol.* **2017**, *29*, 230–244. [CrossRef]
7. Li, X.; Jiang, Y.B.; Zhu, J.C. Air curtain dust-collecting technology: Investigation of industrial application in tobacco factory of the air curtain dust-collecting system. *Process. Saf. Environ. Prot.* **2021**, *149*, 676–683. [CrossRef]
8. Xiao, D.; Li, X.; Yan, W.; Fang, Z. Experimental investigation and numerical simulation of small-volume transverse-flow air curtain performances. *Powder Technol.* **2019**, *352*, 262–272. [CrossRef]
9. Yang, C.S.; An, S.Y.; Chang, W.L. Using air curtain to control pollutant spreading for emergency management in a cleanroom. *Build. Environ.* **2011**, *46*, 1104–1114.
10. Zhao, F.Y.; Shen, G.; Liu, K.J. Room airborne pollutant separation by the use of air curtains in the large building enclosure: Infiltration efficiency and partial enclosure ventilation rate. *J. Build. Eng.* **2018**, *18*, 386–394. [CrossRef]
11. Cao, Z.K.; Han, H.; Gu, B. A novel optimization strategy for the design of air curtains for open vertical refrigerated display cases. *Appl. Therm. Eng.* **2011**, *31*, 3098–3105. [CrossRef]
12. Wang, H.; Qian, H.; Zhou, R. A novel circulated air curtain system to confine the transmission of exhaled contaminants: A numerical and experimental investigation. *Build. Simul.* **2020**, *13*, 1425–1437. [CrossRef] [PubMed]
13. Shu, C.; Wang, L.L.; Zhang, C. Air curtain effectiveness rating based on aerodynamics. *Build. Environ.* **2020**, *169*, 106582. [CrossRef]
14. Yang, S.; Alrawashdehm, H.; Zhang, C. Wind effects on air curtain performance at building entrances. *Build. Environ.* **2019**, *151*, 75–87. [CrossRef]
15. Zhang, H.Z.; Meng, W.J.; Wang, B.B. Research on Gas-solid Two-phase Flow Field Based on CFD-DEM Coupling Simulation in Grab Unloading. *Min. Res. Dev.* **2022**, *42*, 166–172.